lubricants

MDPI

Article

Influence of Water on Tribolayer Growth When Lubricating Steel with a Fluorinated Phosphonium Dicyanamide Ionic Liquid

Luigi A. Urtis [1,2], Andrea Arcifa [2], Peng Zhang [3,†], Junxiao Du [2], Marzia Fantauzzi [1], Daniel Rauber [4], Rolf Hempelmann [4], Tobias Kraus [3,5], Antonella Rossi [1,2,*] and Nicholas D. Spencer [2,*]

1 Department of Chemical and Geological Sciences, University of Cagliari, Campus of Monserrato (CA), I09042 Monserrato, Italy; urtis.lu@unica.it (L.A.U.); fantauzzi@unica.it (M.F.)
2 Laboratory for Surface Science and Technology, Department of Materials, ETH Zurich, Vladimir-Prelog-Weg 5, CH-8093 Zürich, Switzerland; andrea.arcifa@mat.ethz.ch
3 INM—Leibniz Institute for New Materials, Campus D2 2, 66123 Saarbrücken, Germany; zhangpeng3@mail.sysu.edu.cn (P.Z.); Tobias.Kraus@leibniz-inm.de (T.K.)
4 Transfer Center Sustainable Electrochemistry, Saarland University and KIST Europe, Am Markt, Zeile 3, 66125 Saarbrücken, Germany; daniel.rauber@uni-saarland.de (D.R.); r.hempelmann@mx.uni-saarland.de (R.H.)
5 Colloid and Interface Chemistry, Saarland University, Campus D2 2, 66123 Saarbrücken, Germany
* Correspondence: rossi@unica.it or antonella.rossi@mat.ethz.ch (A.R.); nspencer@ethz.ch (N.D.S.)
† Current address: School of Materials Science and Engineering, Key Laboratory for Polymeric Composite and Functional Materials of Ministry of Education, Sun Yat-sen University, Guangzhou 510275, China.

Received: 4 March 2019; Accepted: 19 March 2019; Published: 22 March 2019

Abstract: This work aims to elucidate the role of environmental humidity on the tribological behavior of steel surfaces lubricated with an ionic liquid comprised of a fluorinated phosphonium cation—tributyl-3,3,4,4,5,5,6,6,7,7,8,8,8-tridecafluoro-octyl-phosphonium—and a dicyanamide anion (i.e. $N(CN)_2^-$). Ball-on-disk tribotests were carried out at room temperature and at various levels of relative humidity (RH). Water was found to be required to promote the formation of a tribofilm over the contact area. The reaction layer exhibited a patchy morphology, which resembles that observed formed with conventional antiwear additives such as ZnDTP. A surface-chemical analysis of the tribofilm indicated that the tribofilm is composed of fluorides, oxides, and phosphates, pointing to a stress-induced degradation of the ions and corrosion of the sliding counterparts, which is enabled by the presence of water at the sliding interface.

Keywords: Ionic liquids; tribofilm; mechanochemistry; lubrication; small-area X-ray photoelectron spectroscopy

1. Introduction

Ionic liquids (ILs) are salts with melting points lower than 100 °C, generally comprised of large, asymmetric organic ions. The potential of this class of liquids as lubricants was first recognized by Ye et al. in 2001 [1], who noted that ILs commonly exhibit a number of physical properties—such as low vapor pressure and high thermal stability—that are of interest for lubrication. The promising tribological performance reported in the first publications on IL-mediated lubrication triggered a significant interest among various research groups, as demonstrated by the number of scientific papers available on the topic [2–5]. These tribological investigations are often complemented by the surface-chemical analysis of the tribostressed counterparts, so as to characterize the formation of

a tribofilm resulting from the stress-induced degradation of lubricant and reaction with the solid counterparts [3,6–8]. It is often suggested that these reaction layers may play a central role in reducing friction and preventing wear. However, a detailed picture of the mechanisms leading to their formation has not been presented. In addition, it is often not clear to what degree the presence of these films may affect friction or reduce wear. In this respect, it should be noted that the potential impact of contaminants deriving from the exposure of the IL to air during sliding of IL-lubricated counterparts has been scarcely investigated. This is particularly important in the case of steels, due to the corrosivity of several ILs toward these materials [9–13].

Kondo et al. [14] observed that the exposure to air of self-mated steel lubricated with *N*-methyl-*N*-propyl-piperidinium *bis*(trifluoromethanesulfonyl)imide promoted wear and corrosion of the tribostressed counterparts, suggesting that these adverse effects result from the corrosiveness of hydrogen fluoride, formed by degradation of the fluorinated IL to form FeF_x, and its subsequent hydrolysis in the presence of water. The authors did not discuss the possibility that the presence of a boundary film of adsorbed ions might also play a role in the tribological behavior and that water or other species absorbed from air might affect the composition and properties of the boundary layer.

Recent atomic force microscopy- and surface forces apparatus-based investigations have suggested that water dissolved in ILs can have a strong impact on the properties of a layer of IL confined between polar counterparts [15–19]. In particular, in the case of hydrophobic ILs, water may segregate at the interface between IL and a hydrophilic surface, such as mica or silica [17,20]. Presumably, the phenomenon can occur for a variety of ILs and polar materials, including steels.

In the present work, we investigate the tribological behavior of self-mated 100Cr6 steel lubricated with a hydrophobic fluorinated IL—tributyl-3,3,4,4,5,5,6,6,7,7,8,8,8-tridecafluoro-octyl-phosphonium dicyanamide (F6). The bulk liquid structure, thermal stability and rheological properties of this novel IL, and other homologous compounds, were recently described by Rauber et al. [21]. To date, ILs containing both fluorine and phosphorus in the cation have not been investigated as lubricants. As both the elements may be involved in the formation of protective tribolayers [22], these novel salts may be of interest for tribological application.

Here, the boundary-lubrication properties of F6 are discussed, taking into account the effect of environmental humidity on the reactions leading to tribofilm formation on the tribostressed counterparts.

2. Materials and Methods

2.1. Ionic Liquid

The molecular structure of tributyl-3,3,4,4,5,5,6,6,7,7,8,8,8-tridecafluorooctylphosphonium dicyanamide (F6, in the following) is reported in Figure 1. Details of the synthesis and physical properties of the IL have been presented by Rauber et al. [21].

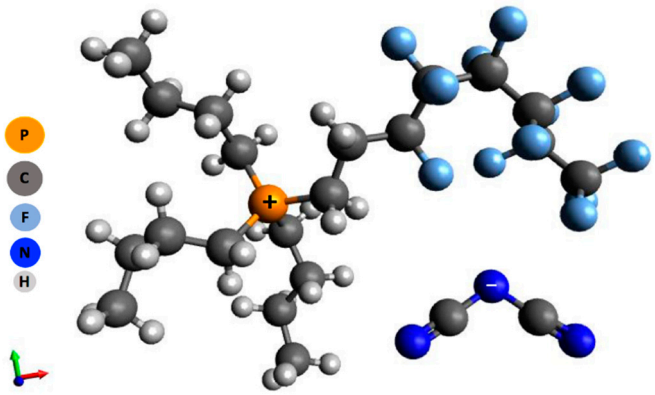

Figure 1. Molecular structure of tributyl-3,3,4,4,5,5,6,6,7,7,8,8,8-tridecafluorooctylphosphonium dicyanamide, the ionic liquid used in this study.

F6 used in tribological testing was characterized by nuclear magnetic resonance, X-ray photoelectron spectroscopy and attenuated-total-reflection Fourier-transform infrared spectroscopy (ATR FTIR). The NMR, XPS, and ATR-FTIR spectra are presented in the Supplementary Materials.

The IL was dehydrated under vacuum and stored under nitrogen in a glovebox. Prior to tribological testing, 0.1 mL of F6 were maintained in contact with the steel sample for 30 min, to enable equilibration with the atmosphere at the desired 1.4 or 5.5 RH%. The IL used for tribological tests at the atmospheric RH% was equilibrated by leaving the vial open during sample mounting.

2.2. Steel Samples

Both the balls and the disks used in the pin-on-disk tribotests were made of 100Cr6 (AISI52100, UNS G52986) steel. The composition of the steel was checked by X-ray fluorescence spectroscopy (XRF) (Table 1). This is a low-alloyed steel.

Table 1. Elemental composition (wt %) of 100Cr6 steel disk determined by XRF. The standard deviation calculated on three independent measurements is reported in parentheses.

100Cr6 Steel	Fe	Cr	C	Mn	Si	S	P
AISI52100	96.5–97.32	1.30–1.60	0.980–1.10	0.250–0.450	0.15–0.30	≤0.0250	≤0.0250
Experimental *	98.10 (6)	1.60 (3)	n.d.	0.30 (1)	<d.l.	<d.l.	<d.l.

"n.d." = not detectable; "d.l." = detection limit; * The technique does not allow the detection of carbon.

The steel disk had a diameter of 20 mm and a height of 8 mm and the ball a diameter of 4.0 mm. The steel disks were polished following the method described in Section 2.3. The steel balls were not mechanically polished prior to the test.

Root-mean-square roughness (Sq) values of 9 ± 2 nm and 14 ± 3 nm were measured for the disks and balls, respectively, using optical profilometry (Section 2.4). The counterparts were rinsed in ethanol (≥99.8%) prior to tribological testing.

2.3. Mechanical Polishing of the Steel Disks

Before the tribological tests, the steel disks were polished according to the Metalog Guide procedure [23]. A Jeanwirtz Phoenix 4000 (Buehler GmBH, Dusseldorf, Germany) rotating polishing wheel was used. The disks were firstly ground with unidirectional rotation at 150 rpm using silicon carbide (SiC)-based grinding papers (Struers GmBH, Willich, Germany) going from the most coarse-grained to the least coarse-grained papers, and subsequently polished by using fine grinding velvet (Struers GmBH) soaked with diamond paste (Struers GmBH). Ethanol (≥99.8%) was used as a lubricant (Table 2) and the disks were sonicated in absolute ethanol for 5 min between each polishing step. The disks were dried under a nitrogen stream.

Table 2. Mechanical polishing steps for the 100Cr6 steel disk.

Step	Type	Speed	Lubricant	Time
Grinding	SiC #500	150 rpm	Ethanol	Until planarity
Grinding	SiC #1200	150 rpm	Ethanol	3'30"
Grinding	SiC #2000	150 rpm	Ethanol	3'30"
Polishing	DP-Plus + 3μm C paste	150 rpm	Ethanol	3'30"
Polishing	DP-Nap + 1 μm C paste	150 rpm	Ethanol	3'30"

2.4. Optical Profilometry

A Sensofar PLu NEOX 3D profilometer (Sensofar-Tech S.L., Terrassa, Spain) was used for investigating the topography of the counterparts. 3D images of the disks were acquired in phase-shifting interferometry (PSI) mode, using a DI 50X-N (NA 0.55) objective.

Extended 3D images of the disk surfaces were acquired by stitching nine 688.24 × 516.26 μm^2 images. 3D images of the spheres were also acquired using the same mode as for the disk (no extended images were acquired in this case).

SensoMAP standard software (v6.2.7106) was used for the analysis of the 3D images. The areal root-mean-square parameters (Sq, the roughness of an areal extension) of the disk were measured after subtracting a least-mean-square plane from the 3D images; in the case of the spheres, a spherical background was subtracted instead.

2.5. Optical Microscopy

Optical images of pins and disks before and after the tribological tests were obtained using an AXIO 10 Imager M1m (Carl Zeiss AG, Oberkochen, Germany) in bright-field mode, equipped with a CCD camera and a 40× magnification lens, and processed with the AxioVs40 software (v4.5.0.0).

2.6. Macrotribological Tests

Tribological tests were carried out using a UMT-2 tribometer (Bruker Nano Inc., Campbell, CA, USA) operating in pin-on-disk mode. A load cell with a maximum capacity of 20 N and resolution of 0.001 N (manufacturer's data) was used for all the experiments.

Tribological tests were carried out at room temperature (21 ± 1 °C) at constant speeds of 1.25 mm/s, applying 5 N load. In addition to tests carried out in the presence of ambient air (35% ± 5% relative humidity, RH), additional tests were performed under controlled environmental conditions. Specifically, a nitrogen atmosphere was produced by placing the tribometer inside a glovebox filled with nitrogen (Labmaster 100, MBraun, Garching, Germany). The effect of the applied load was also investigated; the experiments were carried out at room temperature (21 ± 1 °C) and constant speed (1.25 mm/s), applying 5 N, 10 N and 15 N loads.

Finally, further tests were realized in the presence of air with a low and controlled humidity (1.4 and 5.5% RH). Isolation of the recirculating system of the glovebox and the introduction into the chamber of various mixtures of dry air and laboratory air allowed the achievement of these controlled RH conditions. Prior to any test, 0.1 mL of F6 were placed on the disk.

2.7. Small-area X-ray Photoelectron Spectroscopy (XPS)

X-ray photoelectron spectra of steel balls, before and after tribological testing (and thoroughly rinsing with 2-propanol), were acquired with a PHI Quantera^{SXM} spectrometer (ULVAC-PHI, Chanhassen, MN, USA) equipped with an Al Kα monochromatic source (1486.6 eV) operating in standard-lens mode, and with an emission angle of 45° and directed to the 32-channel detector system.

An electron/ion-beam neutralizer was used to compensate for possible sample charging. The linearity of the binding-energy scale as well as the intensity response function together with the lateral resolution and sharpness were periodically checked using sputter-cleaned gold, silver, copper, and silicon as reference materials; according to ISO 15472:2009 [24] and to ISO/TR 19319 [25].

Since the diameter of the contact area (70 μm) was more than three times the size of the beam used for the analysis (15 μm), the signal originating from the outside of the tribostressed region is expected to contribute less than 10% to the total signal under the conditions described in this work [26].

Survey spectra were acquired in fixed-analyzer-transmission mode, setting the pass energy to 280 eV; the high-resolution spectra were collected setting the pass energy equal to 69 eV.

Afterwards, X-ray-excited, secondary-electron images (SXI) were collected, in order to enable the selection of the points where small-area XP-spectra should be acquired on the ball, following tribological tests. The spectra were corrected with reference to adventitious aliphatic carbon at 285.0 eV (ASTM E 1523–03 Standard Guide to Charge Control and Charge Referencing Techniques in X-Ray Photoelectron Spectroscopy) and were processed using CASAXPS (v2.3.19PR1.0, Casa Software Ltd., Wilmslow, Cheshire, UK).

2.8. Atomic Force Microscopy (AFM)

AFM images were collected in tapping mode by a MFP-3D AFM (Asylum Research, Santa Barbara, CA, USA) using commercial AFM probes (OMCL-AC160TS-R3, Olympus, Tokyo, Japan) consisting of a rectangular cantilever (resonance frequency ca. 300 KHz, typical spring constant ca. 26 N/m) terminated with a sharp tetragonal tip.

2.9. X-ray Fluorescence (XRF)

The 100Cr6 samples were directly analyzed by a hand-held EDXRF SPECTRO xSORT (Spectro Analytical Instruments GmbH, Kleve, Germany) standard-less spectrometer operating in ambient atmosphere. A miniaturized X-ray tube with a Rh anode is mounted in the instrument. The instrument is also equipped with a silicon drift detector (SDD) and an optical integrated video camera for precise spot testing. The X-ray beam can be collimated down to 3 mm. xSORT software (Ametek) is used to control the EDXRF spectrometer. The XRF spectra and quantitative analyses were collected using the manufacturer's "precious metals method" [27]. In order to obtain accurate results for heavy elements, this method requires spectral acquisition at 50 kV and 20 μA.

The instrument was automatically calibrated using the ICAL function [28], which allows the current detector resolution to be determined, calculating the spectrum-energy-correlation and the X-ray intensity. The measurements were performed on three different points for each sample. Each measurement was carried out over a period of up to 60 s.

3. Results

3.1. Tribological Testing

3.1.1. Tribological Testing in Humid Air and in Nitrogen

Figure 2 shows the optical micrographs of steel balls after sliding for 20 minutes against steel disks in the presence of F6 as a lubricant, either in humid air or in a nitrogen atmosphere (Figure 2a and 2b, respectively). The friction traces measured during the tests are presented in Figure 2c.

A visual inspection of the micrographs reveals that the environmental conditions have a significant impact on the appearance of the steel balls after tribotesting. Specifically, a patchy tribofilm was observed over the contact area of samples tribostressed in the presence of humid air (Figure 2a).

In contrast, neither tribofilm formation nor scratches were optically detectable over the contact area of spheres tribostressed in a nitrogen atmosphere (Figure 2b). Similar results were obtained even when increasing the applied load up to 15 N (Supplementary Materials Figure S1). The wear track on tribostressed disks consisted of very mild grooves in the direction of sliding; the track of the disk tested in the presence of humid air is shown in the Supplementary Materials in Figure S2.

The frictional traces of the tests are illustrated in Figure 2c. Tests carried out in the presence of humid air showed that the coefficient of friction increased at the beginning of the test (for about 100–200 s), then slowly decreasing, seemingly approaching a steady state. A more stable trend was observed in the case of tribotests carried out in the presence of a nitrogen atmosphere: no initial transients of friction were observed in this case.

3.1.2. Tribological Testing in Humidity-controlled Environments

Additional tests were carried out at relative humidities of 1.4% RH and 5.5% RH and room temperature (21 ± 1 °C), with the aim of investigating the role of relative humidity on tribolayer formation. All the other parameters were unchanged.

Micrographs of the sphere surface obtained at 1.4% and 5.5% RH show that the tribofilm is formed at the edge of the contact area in both conditions (Figure 3a,b), producing a circular deposit whose radius closely approaches the Hertzian contact radius (40 μm). In the case of the test at 1.4% RH (Figure 3a) a significantly lower amount of tribolayer is formed. Friction traces of the tests described

above are illustrated in Figure 3c. After a short transient at the beginning of the tribotest, a steady state similar to that observed in the nitrogen atmosphere is reached in both cases. These results indicate that the relative humidity influences the amount of tribolayer formed in the contact area of the tribostressed spheres.

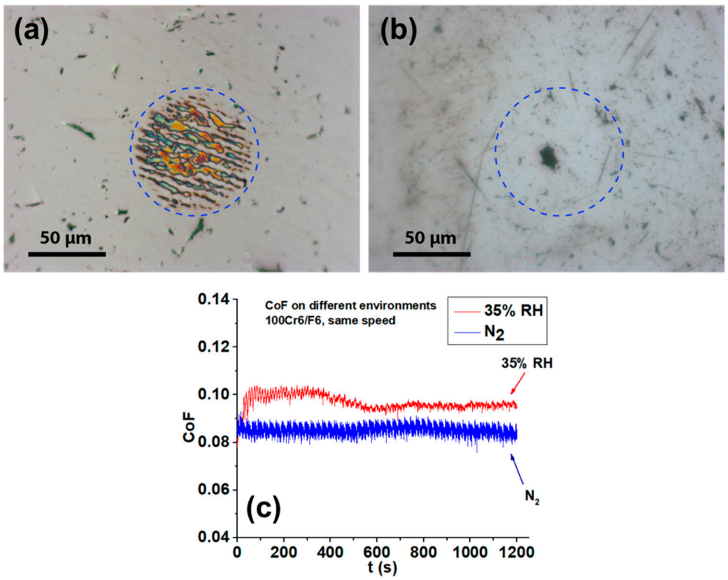

Figure 2. Optical images of 100Cr6 ball after pin-on-disk tribotests using the IL F6 as lubricant, (**a**) in the presence of humid air (35% ± 5% RH) and (**b**) in the nitrogen atmosphere. All tests were carried out with an applied load of 5 N for 20 min at room temperature (21 ± 1 °C). Constant sliding speed: 1.25 mm/s. The corresponding frictional traces are shown in (**c**). Average CoF for the last 200 s: 0.95 ± 0.02 for 35% ± 5% RH-test and 0.83 ± 0.03 for N_2-test. The blue circle indicates the contact area, estimated using Hertzian theory of non-adhesive elastic contact between a self-mated steel sphere and a plane.

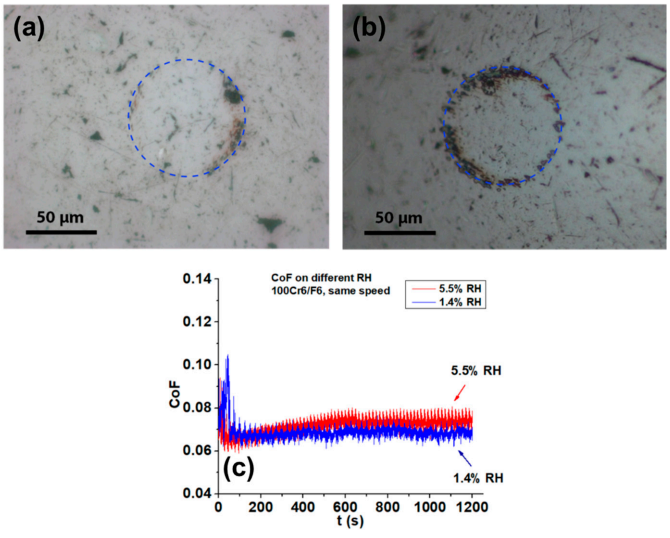

Figure 3. Optical images of 100Cr6 ball after pin-on-disk tribotests using the IL F6 as lubricant and in the presence of dry air at (**a**) 1.4% RH, (**b**) 5.5% RH. All tests were carried out applying a load of 5 N, for a constant sliding speed of 1.25 mm/s and a duration of 20 min at 21 ± 1 °C. The corresponding frictional traces are illustrated in (**c**). Average CoF values calculated over the last 200s were 0.68 ± 0.02 for 1.4% RH test and 0.75 ± 0.02 for 5.5% RH test, respectively. The blue circle indicates the contact area, estimated using Hertzian theory of non-adhesive elastic contact between a self-mated steel sphere and plane.

3.2. AFM Results

AFM topographic images of the ball tribostressed in the presence of humid air are provided in Figure 4. The tribofilm is composed of islands elongated in the sliding direction and up to ~200 nm in height.

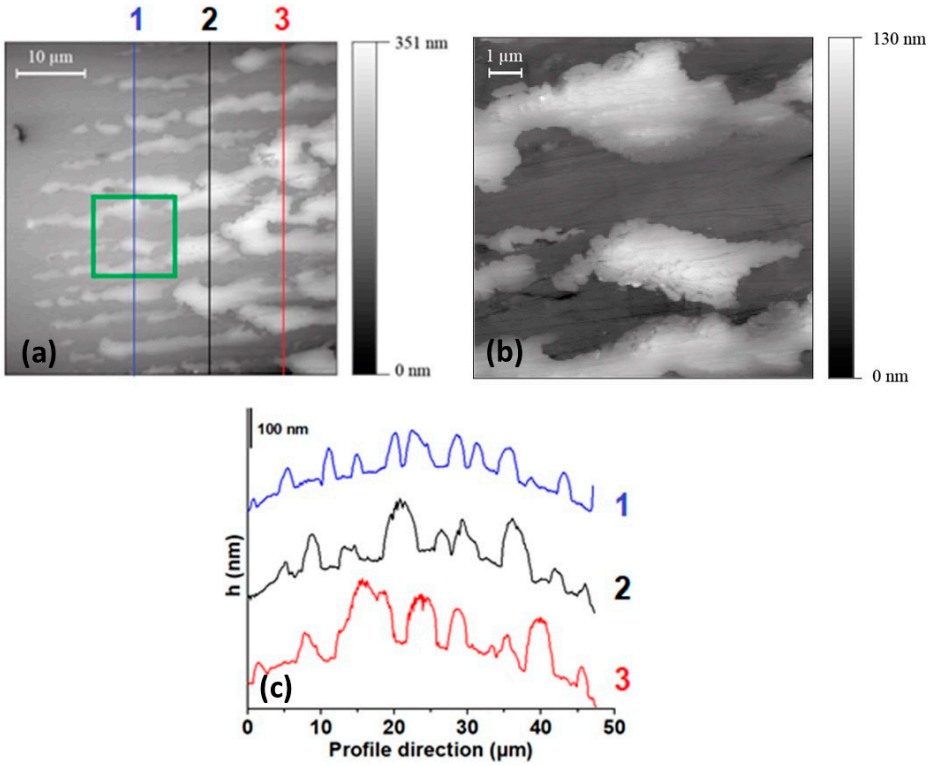

Figure 4. Atomic force microscopy (AFM) height images of the contact area 100Cr6 ball after pin-on-disk tribotests using the ionic liquid (ILs) F6 as lubricant and in presence of humid air (35% ± 5% RH). (**a**) 50 × 50 µm^2 height image of the contact area (**b**) Detail from the green square in (**a**). The test was carried out with an applied load of 5 N and a duration of 20 min at 21 ± 1 °C. Constant sliding speed: 1.25 mm/s. (**c**) Height profiles extracted from the topographical image (Figure 4a).

The extension of these features was found to vary over the contact area, with larger islands being present in the central part of the contact.

3.3. XPS Results

The chemical composition of the deposits formed over the contact area of pins tested in the presence of humid air (Figure 2a) was characterized by X-ray photoelectron spectroscopy. Before the analysis, the samples were thoroughly rinsed with 2-propanol. This cleaning procedure resulted in the removal of IL residues that would otherwise screen the signal from the solid surface underneath.

The spectra acquired on both the contact and non-contact areas are described below. All curve-fitting parameters are listed in the Supplementary Materials (Table S1) together with the apparent concentrations of the chemical species Table S2. For comparison, the XPS spectra of pure F6, which was also characterized by NMR and ATR-FTIR (Figures S3–S9), are provided in the Supplementary Materials (Figures S4 and S5), together with fitting parameters (Table S3) and quantitative analysis (Table S4).

3.3.1. Survey Spectra

Surface characterization started with the identification of the elements present in the part of the sample probed by XPS, estimated to be about 6 nm thick in the present experimental setup.

A survey spectrum was recorded covering a binding-energy range of 0–1200 eV. Photoelectron and Auger peaks were detected and peak identification achieved by means of electron-energy reference tables. Fe 3p, Fe 3s, C 1s, O 1s, Fe 2p, and Fe 2s photoelectron signals and Fe LMM, O KLL, and C KLL Auger-electron signals were revealed, due to the iron substrate and its oxidation products from exposure of the iron surface to the air. The carbon signal resulted from organic species adsorbed on the surface as a consequence of atmospheric exposure during sample introduction into the spectrometer. All these signals were recorded for both non-contact and contact areas (Figure 5). In addition, the survey spectrum, acquired in the contact area, revealed signals attributable to the lubricant (F, N, P). Calcium was also clearly detectable. It should be noted that the concentration of this element in the ionic liquid, determined by ICP-OES, was lower than 10 ppm (Supplementary Materials: Table S5), while its presence on the surface of disk and sphere before the tribotest was found to be lower than 0.1 at %. The significant amount of calcium measured in the contact area points to an enrichment of the element in the tribofilm. The possible origin of the phenomenon is discussed later (Section 4).

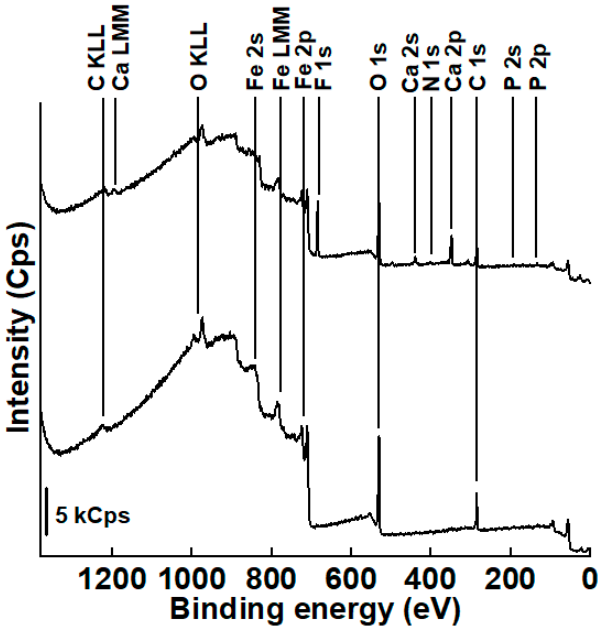

Figure 5. Survey of XP-spectra acquired on the no-contact area (lower plot) and on the contact area (upper plot) of 100Cr6 ball after tribotest (load 5 N, sliding speed 1.25 mm/s, time 20 min, $T = 21 \pm 1$ °C, 35% ± 5% relative humidity (RH)) and 2-propanol rinsing.

3.3.2. High-resolution XP-Spectra

Non-contact Area

Six synthetic Gaussian–Lorentzian curves were used to fit the C 1s signal (Figure 6a): the peak at 283.2 eV is assigned to carbide [29,30] while the components ascribed to aliphatic carbon (BE = 285.0 eV [31]), to C–O and C=O functional groups (286.3 eV [31] and 287.8 eV [8,31]) and carboxyl and carbonates species (288.8 eV) [8,31,32] might be due to the contamination layer typically found on samples exposed to air. The component at BE = 286.3 eV might comprise the signal of C–P bonds [33]. The C–F signal is detected at 290.2 eV [34].

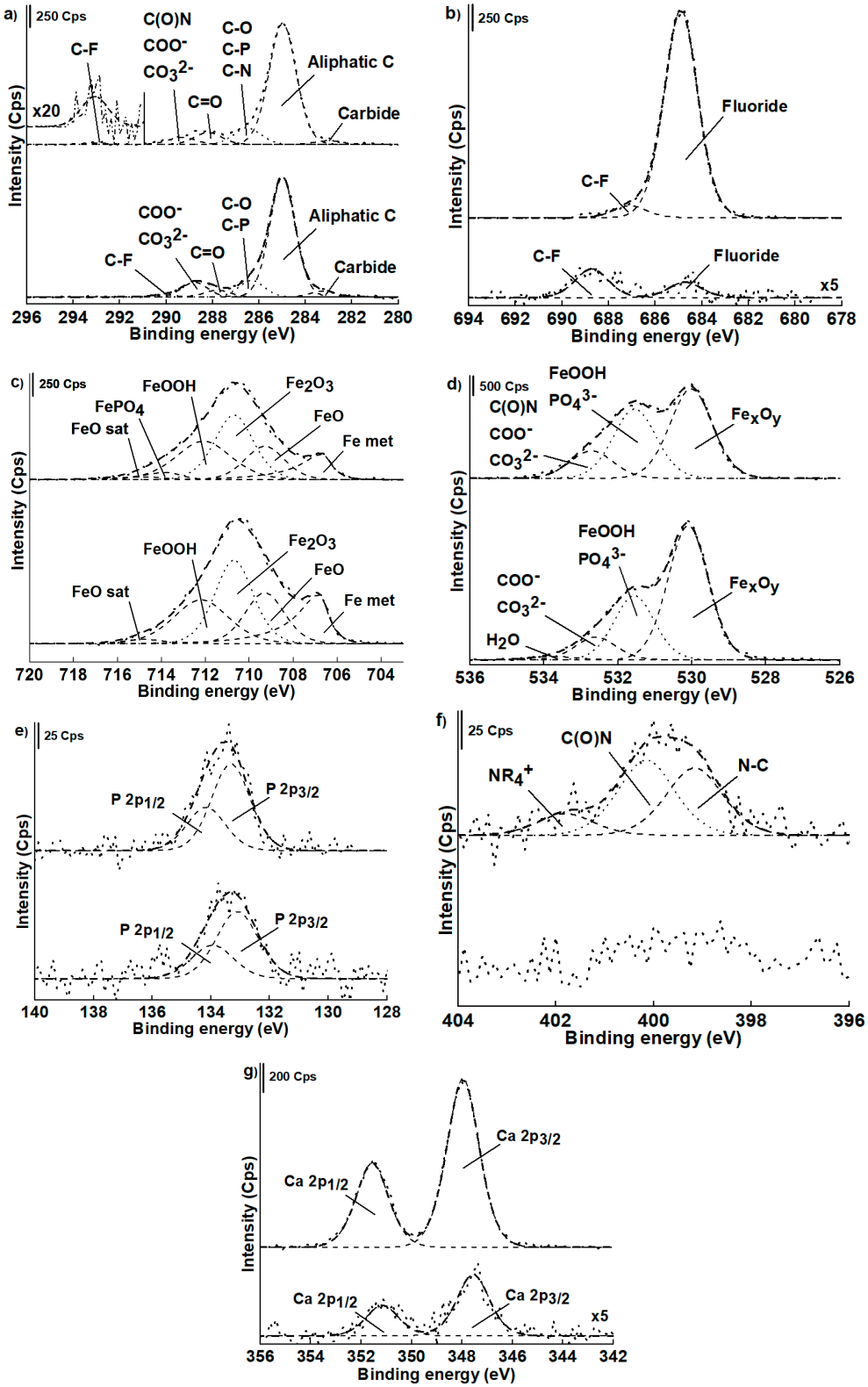

Figure 6. High-resolution X-ray photoelectron spectroscopy (XPS) spectra acquired on the noncontact area (lower plot) and on the contact area (upper plot) of 100Cr6 ball after tribotest (load 5 N, sliding speed 1.25 mm/s, time 20 min, $T = 21 \pm 1$ °C, 35% ± 5% RH) and 2-propanol cleaning. (**a**) C 1s, (**b**) F 1s, (**c**) Fe $2p_{3/2}$, (**d**) O 1s, (**e**) P 1s, (**f**) N 1s, and (**g**) Ca 2p.

The F 1s signal shows two components (Figure 6b) that could be related to the presence of C–F (688.7 eV) [34] and to metallic fluoride (684.7 eV) [35].

The Fe $2p_{3/2}$ spectrum was fitted by six components (Figure 6c) and they were assigned to metallic iron at 706.8 eV [30,32], Fe(II) oxide and its satellites at 709.3 eV and 714.8 eV respectively [30,32,36], Fe(III) oxide at 710.7 eV [30,32,36], and Fe(III) oxy-hydroxide at 712.2 eV [30,32].

The oxygen, O 1s signal was resolved in four components (Figure 6d). The first one is found at 530.1 eV, and is due to iron oxides [30,32]. The peak at 531.6 eV is ascribed to hydroxides [30,32] and phosphates [37,38]: their presence is also confirmed by the P signal. The O 1s component at BE = 532.6 eV is attributed to oxygen of carbonyl and carbonates (532.6 eV) [30,32]. The fourth component at 533.8 eV can be assigned to the oxygen of adsorbed water [32]. The P 2p signal consists of a doublet due to spin-orbit coupling. The most intense P $2p_{3/2}$ peak is found at 133.1 eV; the energy separation $2p_{3/2}$–$2p_{1/2}$ is found to be 0.84 eV and their area ratio is 2:1 (Figure 6e); it may be attributable to phosphates [37,38].

No curve fitting of N 1s was attempted due to the low signal-to-noise ratio (Figure 6f).

The Ca 2p signal is a doublet with the Ca $2p_{3/2}$ component at 347.6 eV and the Ca $2p_{1/2}$ separated by 3.6 eV at 351.2 eV (Figure 6g) and it may be due to calcium fluoride (347.5 $\pm$ 0.2 eV) [39], calcium carbonate (347.7 $\pm$ 0.2 eV) [40] or calcium phosphate (347.3 $\pm$ 0.2 eV) [38].

Contact Area

Six components were used to fit the C 1s signal (Figure 6a): carbide (283.0 eV) [29,30], aliphatic hydrocarbon (285.0 eV) [31], ether [31], C–P [33] and C–N moieties (286.5 eV), carbonylic [41] and amidic carbon (288.2 eV), and carboxyl and carbonates species (289.3 eV) [8,31,32], and C–F bearing groups (293.1 eV) [42].

The F 1s signal was fitted by two components (Figure 6b), one assigned to C–F (687.1 eV) and the other to metallic fluoride (684.9 eV) [35]. This last peak dominates the spectra of the contact area, indicating that metallic fluorides are the main species of the tribolayer. Notably, the peak maximum signal is not centered at the binding-energy value expected for iron (II) or iron (III) fluorides (685.5 eV and 686.2 eV, respectively, Figures S6 and S7 of the Supplementary Materials); it more closely approaches the value of calcium fluorides [39]. In addition, the ratio of the apparent concentrations estimated for calcium and fluorine is 1.5, suggesting that CaF_2 is the main product responsible for the observed signal—although a minor contribution from iron fluoride cannot be ruled out.

The Fe $2p_{3/2}$ spectrum can be fitted by six species (Figure 6c): metallic iron (706.7 eV) [30,32], Fe(II) oxide (709.3 eV) and its satellites (714.8 eV) [30,32,36], Fe(III) oxide (710.7 eV) [30,32], Fe(III) oxy-hydroxide (712.1 eV) [30,32], and Fe(III) phosphate (713.7 eV) [43]. Although an analysis of the F 1s signal suggests that most of the fluorine at the surface is bonded with calcium, a contribution of iron fluorides to the Fe 2p signal cannot be excluded.

However, these contributions to the XP-iron spectrum are difficult to differentiate from those of oxides and phosphates.

The O 1s signal was resolved by fitting three components (Figure 6d): oxygen from metal oxides (530.0 eV) [30,32], oxygen in hydroxides [30,32] and phosphates [37,38] (531.6 eV), oxygen from carbonyl, carbonates, and amidic groups (532.7 eV) [30,32]. The P 2p spectrum is a doublet with the P $2p_{3/2}$ peak at 133.3 eV and the P $2p_{1/2}$ at 134.2 eV (Figure 6e); this signal might suggest the presence of phosphates [37,38]. The N 1s spectrum is resolved by fitting three components (Figure 6f): amines [44] (399.2 eV), amidic groups (400.2 eV) [41,44] and quaternary ammonium cations (401.8 eV) [41].

The doublet for the Ca spectrum presents a component at 348.0 eV (Ca $2p_{3/2}$) and another component at 351.6 eV (Ca $2p_{1/2}$) (Figure 6g); it might be associated with the presence of several Ca bearing compounds, such as: calcium fluoride [39], calcium carbonate [40], or calcium phosphate [38].

4. Discussion

The experiments presented in this work were carried out under conditions of negligible wear, such that the sphere-on-plane geometry of the contact of the counterparts did not change significantly as a result of sliding. For this geometry, the Hamrock and Dowson formula [45] can be used to predict the regime of lubrication [46]. According to the calculation reported in Section S7 (Figure S10 and Table S6), a λ ratio—the ratio between the minimum film thickness and the composite roughness of the tribopair [46–48]—of approximately 0.2 is estimated, suggesting that the tribological behavior is mostly related to interaction between asperities (boundary lubrication).

Under these conditions, it appears that environmental effects dictate the formation of a tribolayer on the contact area of 100Cr6 steel counterparts during sliding in the presence of F6. A patchy tribolayer was formed on the pin surface in the presence of humid air. Its appearance and morphology show some similarity with those observed for steels lubricated with engine oils containing antiwear additives (AW), such as zinc dialkyldithiophosphate (ZnDTP) [8,49].

For comparison, a tribotest was carried out for the same steel counterparts in the presence of a hydrocarbon oil (Viscosity and Density Reference Standard, ISO 17025, Paragon Scientific LTD., Prenton, UK) with ZnDTP as an additive (2 wt %). An optical micrograph of the tribolayer formed at the surface of the pin after tribotesting is reported in Figure 7.

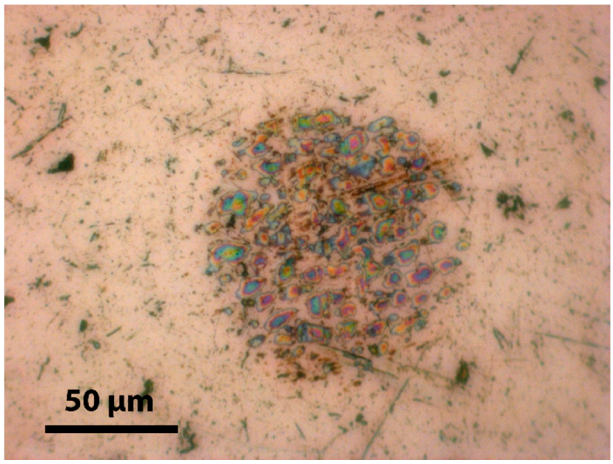

Figure 7. Optical images of 100Cr6 ball after pin-on-disk tribotests using a hydrocarbon oil with zinc dialkyldithiophosphate (ZnDTP) additive (2 wt %) as lubricant and in presence of humid air (35% ± 5% RH). The test was carried out with an applied load of 5 N and a duration of 20 min at 21 ± 1 °C. Constant sliding speed: 24.0 mm/s.

In the present work, no tribolayer formation was observed for the IL-lubricated counterparts sliding in a nitrogen atmosphere (Figure 2b). We infer that the ionic liquid is able to prevent severe wear of self-mated steel—at least in the case of highly polished counterparts (composite roughness Sq = 17 ± 2 nm, Section S7).

In contrast, exposure to humid air resulted in a tribofilm formation and was associated with a small increase of the CoF value, as well as the appearance of wear. Both these phenomena seem to indicate that the presence of water in F6 could disturb the mechanism of boundary lubrication.

It is worth noting that a number of recent studies suggest that water can indeed segregate at the surface of polar solids, such as silica [15,18,20] or mica [17,18]. Possibly, a similar phenomenon might also occur in the case of steels: mechanically polished surfaces are found to exhibit 3–5 nanometers thick oxy-hydroxide layers [50,51]. This finding is also supported by the XPS results obtained on the non-contact area. This layer being polar may act similarly to the surface of silica and mica.

The presence of water could also affect the mechanochemical reactions that are responsible for tribofilm formation. The XPS analysis of the tribolayer indicates that degradation products of the ionic

liquid are found in the reaction layer; no signals attributable to the presence of the unaltered ionic liquid could be detected. In addition, the analysis of the Fe 2p signals indicate that humid air promotes oxidation of steel at the sliding interface, as the area ratios between the components due to metallic iron and to oxidised iron in Fe $2p_{3/2}$ signals, is higher in the contact than in the non-contact area (0.15 and 0.24, respectively).

The enrichment of water at the sliding interface might also explain the detection of calcium in the tribolayer. Chemical analysis of F6 (Supplementary Materials: Sections S4 and S5), and the surface-chemical analysis of the steel counterparts prior to the tests (Figures S11–S14, Tables S7 and S8) indicate that this element, if present, is below the detection limit under the adopted conditions. The presence of water at the sliding interface might promote the segregation of traces of calcium at the sliding interface, facilitating the inclusion of the element in the tribofilm. As mentioned in Section 3.3, most of the Ca^{2+} seems to precipitate as CaF_2.

Other inorganic anions compounds were found in the tribolayer, such as phosphates, carbonates, and hydroxides, all of which contain oxygen. The formation of these compounds agrees with the stress-induced degradation of the ionic liquid ions and oxidation of the steel surfaces.

The presence of CaF_2 limits the formation of iron fluorides and, since CaF_2 is stable in contact with water, there is no formation of HF. Consequently, the corrosiveness of F6 is lower than that of typical halogen-bearing ILs. Among halogen-free dicyanamide ionic liquids, [EMIM][DCN] has been reported to cause corrosion when tests were carried out at room temperature in humid air [52], and its performance as a lubricant has been found to be inferior to that of fluorine-containing ILs [14]. In contrast, the novel phosphonium dicyanamide investigated in this study exhibits a low coefficient of friction and negligible wear.

The analysis of optical micrographs and AFM images reveals that the tribolayer formed in the presence of a sufficiently high humidity level (35% $\pm$ 5% RH, Figure 2a) is composed of island-like structures, whose extension is higher at the center of the elastically deformed contact area. This finding might indicate that the mechanochemical reaction leading to tribofilm growth is accelerated by the local pressure [53], which is higher at the center of the contact area.

On the other hand, it was also observed that the growth of the tribolayer was limited to the border of the contact area when tests were carried out at low humidity, i.e. below ~5% RH (Figure 3a). This behavior might suggest that the diffusion of water toward the sliding interface might play an important role in affecting the tribofilm formation: depletion of this reactant in the confined IL might occur if the diffusion rate of water toward the sliding interface is higher than the rate of its consumption by mechanochemical reaction.

Finally, it should be noted that degradation products of the IL cation and anion, such as phosphates and fluorides, were also found in small amounts in the non-contact area, where the action of mechanical stresses can be excluded. The presence of these species might be related to the release of reaction products from the contact area. On the other hand, the XPS analysis of steel disks covered by the IL and exposed to humid air for 1 h (Section S8) revealed that small amounts of degradation products of the IL are formed on the surface of the undamaged disk, indicating that the reaction can also occur in the absence of mechanical stress.

5. Conclusions

The formation of a tribolayer at the sliding interface of F6-lubricated steel counterparts is the result of stress-promoted mechanochemical reactions that involve iron, the ionic liquid, and species that are present in the IL as result of exposure to humid air. In particular, water was found to be a required reactant for the formation and growth of a tribolayer, which was mostly composed of oxidic products of iron and metallic fluorides. Calcium, a trace impurity, was detected in significant amounts in the tribolayer, mostly in the form of CaF_2. This may be the result of segregation of the ionic contaminant at the water-enriched solid-liquid interface.

The morphology of the tribofilm formed on F6-lubricated steel in the presence of humid air shows similarities to those of reaction layers formed by conventional antiwear additives. Thicker and larger islands are present in the center of the contact area, suggesting that contact pressure promotes the tribochemical reactions. The diffusion of water toward the sliding interface might also play an important role in affecting the morphology of the reaction film, as the growth of the tribolayer during tests carried out in the presence of dry air (RH $\leq$ 5.5%) was limited to the border of the contact area.

The simultaneous presence of fluorine and phosphorus provides F6 with the good lubricant properties that are typical of halogen-bearing ILs and the corrosion-inhibiting properties of phosphonium based-ILs.

Supplementary Materials: Supplementary Materials are available online at http://www.mdpi.com/2075-4442/7/3/27/s1.

Author Contributions: L.A.U.: Performing X-ray photoelectron spectroscopy and tribological experiments; processing the data; writing the manuscript; A.A.: Methodological design of the research; atomic force microscopy (AFM) image acquisition; writing the manuscript; mentorship and consultation; paper revision prior to submission; P.Z.: ICP-OES experiment, project coordination, and paper revision prior to submission; J.D.: Feasibility tribological studies, and tribological experiments in the presence of controlled humidity; M.F.: XPS data processing and interpretation; writing the paper; XRF steel characterization; paper revision prior to submission; D.R.: Ionic liquid synthesis and characterization; paper revision prior to submission; R.H.: Mentorship and consultation, grant and funding acquisition, paper revision prior to submission; T.K.: Mentorship and consultation, initial project design, paper revision prior to submission; A.R.: Design of the research; research methods selection, data interpretation, conclusions, mentorship and consultation; paper revision prior to submission; N.D.S.: Mentorship and consultation, paper revision prior to submission.

Funding: This research was funded by Fondazione Banco di Sardegna and Regione Autonoma della Sardegna Progetti Biennali di Ateneo Annualità 2016; grant number Fondazione Sardegna CUP F72F16003070002.

Acknowledgments: P. Zhang and T. Kraus acknowledge the continuing support of Eduard Arzt for this project. The authors wish to express their gratitude to Giovanni Cossu for the calibration of the spectrometer and to Michele Aldeghi for the preliminary measurements carried out during his BS work (Spring semester 2017).

Conflicts of Interest: The authors declare no conflict of interest.

References

1. Ye, C.; Liu, W.; Chen, Y.; Yu, L. Room-temperature ionic liquids: A novel versatile lubricant. *Chem. Commun.* **2001**, *21*, 2244–2245. [CrossRef]
2. Bermúdez, M.-D.; Jiménez, A.-E.; Sanes, J.; Carrión, F.-J. Ionic liquids as advanced lubricant fluids. *Molecules* **2009**, *14*, 2888–2908. [CrossRef] [PubMed]
3. Minami, I. Ionic Liquids in Tribology. *Molecules* **2009**, *14*, 2286–2305. [CrossRef] [PubMed]
4. Somers, A.E.; Howlett, P.; MacFarlane, D.; Forsyth, M. A Review of Ionic Liquid Lubricants. *Lubricants* **2013**, *1*, 3–21. [CrossRef]
5. Xiao, H. Ionic Liquid Lubricants: Basics and Applications. *Tribol. Trans.* **2017**, *1*, 20–30. [CrossRef]
6. Martin, J.M.; Grossiord, C.; Le Mogne, T.; Bec, S.; Tonck, A. Role of nitrogen in tribochemical interaction between ZnDDP and succinimide in boundary lubrication. *Tribol. Int.* **2001**, *34*, 523–530. [CrossRef]
7. Eglin, M.; Rossi, A.; Spencer, N.D. X-ray photoelectron spectroscopy analysis of tribostressed samples in the presence of ZnDTP: A combinatorial approach. *Tribol. Lett.* **2003**, *15*, 199–209. [CrossRef]
8. Nedelcu, I.; Piras, E.; Rossi, A.; Pasaribua, H.R. XPS analysis on the influence of water on the evolution of zinc dialkyldithiophosphate-derived reaction layer in lubricated rolling contacts. *Surf. Interface Anal.* **2012**, *44*, 1219–1224. [CrossRef]
9. Maton, C.; De Vos, N.; Steven, C.V. Ionic liquid thermal stabilities: Decomposition mechanisms and analysis tools. *Chem. Soc. Rev.* **2013**, *42*, 5963–5977. [CrossRef]
10. Minami, I.; Kamimura, H.; Mori, S. Thermo-oxidative stability of ionic liquids as lubricating fluids. *J. Synth. Lubr.* **2007**, *24*, 135–147. [CrossRef]
11. Molchan, I.; Thompsopn, G.; Walton, J.; Skeldon, P.; Tempez, A.; Legendre, S. Passivation behaviour of 304 stainless steel in an ionic liquid with a fluorinated anion. *Appl. Surf. Sci.* **2015**, *357*, 37–44. [CrossRef]
12. Perissi, I.; Bardi, U.; Caporali, S.; Lavacchi, A. High temperature corrosion properties of ionic liquids. *Corros. Sci.* **2006**, *48*, 2349–2362. [CrossRef]

13. Gabler, C.; Tomastick, C.; Brenner, J.; Pisarova, L.; Doerr, N.; Allmaier, G. Corrosion properties of ammonium based ionic liquids evaluated by SEM–EDX, XPS and ICP-OES. *Green Chem.* **2011**, *13*, 2869–2877. [CrossRef]
14. Kondo, Y.; Yagi, S.; Koyama, T.; Tsuboi, R.; Sasaki, S. Lubricity and corrosiveness of ionic liquids for steel-on-steel sliding contacts, Proceedings of the Institution of Mechanical Engineers. *J. Eng. Tribol.* **2012**, *226*, 991–1006.
15. Espinosa-Marzal, R.M.; Arcifa, A.; Rossi, A.; Spencer, N.D. Ionic liquids confined in hydrophilic nanocontacts: Structure and lubricity in the presence of water. *J. Phys. Chem. C* **2014**, *118*, 6491–6503. [CrossRef]
16. Espinosa-Marzal, R.M.; Arcifa, A.; Rossi, A.; Spencer, N.D. Microslips to "avalanches" in confined, molecular layers of ionic liquids. *J. Phys. Chem. Lett.* **2013**, *5*, 179–184. [CrossRef]
17. Sakai, K.; Okada, K.; Uka, A.; Misono, T.; Endo, T.; Sasaki, S.; Abe, M.; Sakai, H. Effects of water on solvation layers of imidazolium-type room temperature ionic liquids on silica and mica. *Langmuir* **2015**, *31*, 6085–6091. [CrossRef]
18. Cheng, H.-W.; Dienemann, J.N.; Stock, P.; Merola, C.; Chen, Y.J.; Valtiner, M. The Effect of Water and Confinement on Self-Assembly of Imidazolium Based Ionic Liquids at Mica Interfaces. *Sci. Rep.* **2016**, *6*, 30058. [CrossRef] [PubMed]
19. Jurado, L.A.; Kim, H.; Rossi, A.; Arcifa, A.; Schuh, J.K.; Spencer, N.D.; Leal, C.; Ewoldt, R.H.; Espinosa-Marzal, R.M. Effect of the environmental humidity on the bulk, interfacial and nanoconfined properties of an ionic liquid. *Phys. Chem. Chem. Phys.* **2016**, *18*, 22719–22730. [CrossRef]
20. Arcifa, A.; Rossi, A.; Ramakrishna, S.N.; Espinosa-Marzal, R.S.; Spencer, N.D. Lubrication of Si-Based Tribopairs with a Hydrophobic Ionic Liquid: The Multiscale Influence of Water. *J. Phys. Chem. C* **2018**, *122*, 7331–7343. [CrossRef]
21. Rauber, D.; Zhang, P.; Huch, V.; Kraus, T.; Hempelmann, R. Lamellar structures in fluorinated phosphonium ionic liquids: The roles of fluorination and chain length. *Phys. Chem. Chem. Phys.* **2017**, *19*, 27251–27258. [CrossRef]
22. Minami, I.; Inada, T.; Sasaki, R.; Nanao, H. Tribo-chemistry of phosphonium-derived ionic liquids. *Tribol. Lett.* **2010**, *40*, 225–235. [CrossRef]
23. Struers A/S. *Struers A/S Metalog Guide*; Struers A/S: Rødovre, Denmark, 2002; ISBN 87-987767-0-3.
24. ISO. *ISO 15472:2010 Surface Chemical Analysis—X-ray Photoelectron Spectrometers—Calibration of Energy Scales*; ISO: Geneva, Switzerland, 2010.
25. ISO. *ISO/TR 19319 Surface Chemical Analysis—Fundamental Approaches to Determination of Lateral Resolution and Sharpness in Beam-Based Methods*; ISO: Geneva, Switzerland, 2013.
26. Passiu, C.; Rossi, A.; Bernard, L.; Paul, D.; Hammond, J.; Unger, W.E.S.; Venkataraman, N.V.; Spencer, N.D. Fabrication and Microscopic and Spectroscopic Characterization of Planar, Bimetallic, Micro-and Nanopatterned Surfaces. *Langmuir* **2017**, *33*, 5657–5665. [CrossRef]
27. SPECTRO Analytical Instruments GmbH. *Analysis of Solid Metal Samples*; Nr. XRF-70, Rev. 2; SPECTRO Analytical Instruments GmbH: Kleve, Germany, 2011.
28. SPECTRO Analytical Instruments GmbH. *Handheld XRF Spectrometer—Original Operating Instructions*; SPECTRO Analytical Instruments GmbH: Kleve, Germany, 2016.
29. Wiltner, A.; Linsmeier, C. Formation of endothermic carbides on iron and nickel. *Phys. Status Solidi A* **2004**, *201*, 881–887. [CrossRef]
30. Mangolini, F.; Rossi, A.; Spencer, N. Influence of metallic and oxidized iron/steel on the reactivity of triphenyl phosphorothionate in oil solution. *Tribol. Int.* **2011**, *44*, 670–683. [CrossRef]
31. Mangolini, F.; Rossi, A.; Spencer, N.D. Tribochemistry of triphenyl phosphorothionate (TPPT) by in situ attenuated total reflection (ATR/FT-IR) tribometry. *J. Phys. Chem. C* **2012**, *116*, 5614–5627. [CrossRef]
32. Elsener, B.; Pisu, M.; Fantauzzi, M.; Addari, D.; Rossi, A. Electrochemical and XPS surface analytical study on the reactivity of Ni-free stainless steel in artificial saliva. *Mater. Corros.* **2016**, *6*, 591–599. [CrossRef]
33. Blundell, R.K.; Licence, P. Quaternary ammonium and phosphonium based ionic liquids: A comparison of common anions. *Phys. Chem. Chem. Phys.* **2014**, *16*, 15278–15288. [CrossRef]
34. Ferraria, A.M.; da Silva, J.D.L.; Botelho do Rego, A.M. XPS studies of directly fluorinated HDPE: Problems and solutions. *Polymer* **2003**, *44*, 7241–7249. [CrossRef]
35. Murch, G.E.; Thorn, R.J. Relation between orbital binding energies and ionicities in alkali and alkaline earth flourides. *J. Phys. Chem. Solids* **1980**, *41*, 785–791. [CrossRef]

36. Fantauzzi, M.; Pacella, A.; Atzei, D.; Gianfagna, A.; Andreozzi, G.B.; Rossi, A. Combined use of X-ray photoelectron and Mössbauer spectroscopic techniques in the analytical characterization of iron oxidation state in amphibole asbestos. *Anal. Bioanal. Chem.* **2010**, *396*, 2889–2898. [CrossRef] [PubMed]
37. Crobu, M.; Rossi, A.; Mangolini, F.; Spencer, N.D. Chain-length-identification strategy in zinc polyphosphate glasses by means of XPS and ToF-SIMS. *Anal. Bioanal. Chem.* **2012**, *403*, 1415–1432. [CrossRef]
38. Ide-Ektessabi, A.; Yamaguchi, T.; Tanaka, Y. RBS and XPS analyses of the composite calcium phosphate coatings for biomedical applications. *Nucl. Instrum. Methods Phys. Res. B* **2005**, *241*, 685–688. [CrossRef]
39. Nefedov, V.I.; Salyn Ya, V.; Leonhardt, G.; Scheibe, R. A comparison of different spectrometers and charge corrections used in X-ray photoelectron spectroscopy. *J. Electron Spectrosc. Relat. Phenom.* **1977**, *10*, 121–124. [CrossRef]
40. Stipp, S.L.S.; Hochella, M.F., Jr. Structure and bonding environments at the calcite surface as observed with X-ray photoelectron spectroscopy (XPS) and low energy electron diffraction (LEED). *Geochim. Cosmochim. Acta* **1991**, *55*, 1723–1736. [CrossRef]
41. Atzei, D.; Fantauzzi, M.; Rossi, A.; Fermo, P.; Piazzalunga, A.; Valli, G.; Vecchi, R. Surface chemical characterization of PM10 samples by XPS. *Appl. Surf. Sci.* **2014**, *307*, 120–128. [CrossRef]
42. Nansé, G.; Papirer, E.; Fioux, P.; Moguet, F.; Tressaud, A. Fluorination of carbon blacks: An X-ray photoelectron spectroscopy study: I. A literature review of XPS studies of fluorinated carbons. XPS investigation of some reference compounds. *Carbon* **1997**, *35*, 175–194. [CrossRef]
43. Crobu, M. Synthesis, Characterization and Tribochemical Behavior. Ph.D. Thesis, ETH Zurich, Zürich, Switzerland, 2012.
44. Rouxhet, P.G.; Genet, M.J. XPS analysis of bio-organic systems. *Surf. Interface Anal.* **2011**, *43*, 1453–1470. [CrossRef]
45. Hamrock, B.J.; Dowson, D. Isothermal Elastohydrodynamic Lubrication of Point Contacts: Part III—Fully Flooded Results. *J. Lubr. Technol.* **1977**, *99*, 264–275. [CrossRef]
46. Tallian, T.E. On competing failure modes in rolling contact. *ASLE Trans.* **1967**, *10*, 428–439. [CrossRef]
47. Stachowiak, G.; Batchelor, A.W. *Engineering Tribology*; Butter Worth-Heinemann: Oxford, UK, 2013.
48. Moyer, C.A.; Bahney, L.L. Modifying the Lambda Ratio to Functional Line Contacts. *Tribol. Trans.* **1990**, *33*, 535–542. [CrossRef]
49. Ghanbarzadeh, A.; Piras, E.; Nedelcu, I.; Brizmer, V.; Wilson, M.C.T.; Morina, A.; Dowson, D.; Neville, A. Zinc dialkyl dithiophosphate antiwear tribofilm and its effect on the topography evolution of surfaces: A numerical and experimental study. *Wear* **2016**, *362–363*, 186–198. [CrossRef]
50. Olla, M.; Navarra, G.; Elsener, B.; Rossi, A. Nondestructive in-depth composition profile of oxy-hydroxide nanolayers on iron surfaces from ARXPS measurement. *Surf. Interface Anal.* **2006**, *38*, 964–974. [CrossRef]
51. Heuberger, R.; Rossi, A.; Spencer, N.D. Reactivity of alkylated phosphorothionates with steel: A tribological and surface-analytical study. *Lubr. Sci.* **2008**, *20*, 79–102. [CrossRef]
52. Kawada, S.; Sasaki, S. Tribological Properties of Cyan-based Ionic Liquids under Different Environments. *Tribol. Online Jpn. Soc. Tribol.* **2018**, *13*, 152–156. [CrossRef]
53. Gosvami, N.N.; Bares, J.A.; Mangolini, F.; Konicek, A.R.; Yablon, D.G.; Carpick, R.W. Mechanisms of antiwear tribofilm growth revealed in situ by single-asperity sliding contacts. *Science* **2015**, *348*, 102–106. [CrossRef]